Ferromagnetic Ni Nanoparticle with Controlled Anisotropy: From Polyhedral to Planar Tetrapods

Georgiana Maties, Marion Luu, Kosseila Ait-Oukaci, Ilona Lecerf, Cécile Marcelot, Anaïs Fondet, Simon Cayez, Christophe Gatel, Thomas Blon, Bruno Chaudret, et al.

Ferromagnetic Ni Nanoparticle with Controlled Anisotropy : from Polyhedral to Planar Tetrapods

Georgiana Maties,[1] Marion Luu, [1] Kosseila Ait-Oukaci, [1] Ilona Lecerf,[1] Cécile Marcelot,[2] Anaïs Fondet,[2] Simon Cayez, [1] Christophe Gatel,[2] Thomas Blon,[1] Bruno Chaudret, [1] Lise-Marie Lacroix[1,3]*

1. Université de Toulouse, Laboratoire de Physique et Chimie des Nano-Objets, UMR 5215 INSA, CNRS, UPS, 135 avenue de Rangueil 31077 Toulouse, France

2. CEMES-CNRS, 29 rue Jeanne Marvig, 31055 Toulouse, France

3. Institut Universitaire de France (IUF), 103 boulevard Saint Michel, 75005 Paris, France

ABSTRACT. Liquid phase syntheses mainly yield nanoparticles with compact shapes, such as spheres or cubes. However, controlling not only the size but also the shape of magnetic nanoparticles would enable a fine tuning of their intrinsic properties, due to the shape anisotropy induced by long-range dipolar interactions. We report here a fairly simple approach based on the reduction of an amidinate complex in presence of a mixture of long chains acid and amine to yield ferromagnetic Ni nanoparticles. The formation of stable Ni complexes could be promoted *in situ* by increasing the acid concentration, thus allowing to tune the final particle size. While amine could be use as soft reducing agent, dihydrogen was essential to promote anisotropic shapes. Electron holography combined with micromagnetic simulations showed that the resulting shape anisotropy could impose complex magnetic configurations within planar tetrapods. Regarding the heating efficiency, which directly scales with the magnetic hysteresis loop area, maxima of $100 W.g^{-1}$ were found for nanoplates and nanorods, opening promising perspectives for magnetically-induced catalysis.

INTRODUCTION.

The control of the size, shape and surface state of metallic nanoparticles has been a long-sought goal for the last decades due to their key impact on both physical and chemical properties of the particles. Controlling the individual properties of nanoparticles is a prerequisite for developing *ad-hoc* nanostructured materials for a given applications. In the case of magnetic particles, the superparamagnetic state, where the reversal of the magnetic moments is thermally activated, is only observed at small sizes. For larger particles, a "frozen" ferromagnetic state is observed, the transition between these two regimes being quite abrupt and strongly depends on the material.[1] For efficient radiofrequency filters, which are implemented in every mobile phone, a soft ferromagnetic material with large permeability and no coercivity is highly desired.[2] Thus, superparamagnetic building blocks with high magnetization should be used. Recently, magnetic nanoparticles have been widely developed for magnetic hyperthermia and magnetically-induced catalysis due to their ability to serve as localized heat mediators once exposed to an alternative magnetic field.[3,4,5] To optimize the heating efficiency, quantified by the Specific Absorption Rate, single-domain ferromagnetic NPs exhibiting a moderate coercive field should be preferred.[6]

The superparamagnetic/ferromagnetic transition is governed by the Neel relaxation time

$$\tau_N = \tau_0 exp\left(\frac{K_{eff}V}{k_BT}\right) \text{ (Eq. 1)},$$[6]

with τ_0 the attempt time, k_BT the thermal energy and $K_{eff}V$ the energy barrier to overpass, dictated by the NP volume V and the effective anisotropy constant K_{eff} which results from the

magnetocrystalline, shape and surface contributions. Therefore, one needs to control the size and the shape of the NP to finely tune the magnetic properties. One of the pioneer work on the size control of magnetic nanoparticles was reported by Prof. Horst Weller's group on $CoPt_3$ NPs, among 20 years ago.[7] They demonstrated that, in the absence of Ostwald ripening, the final NP size was dictated by the balance between the nucleation and growth rates. By adding carboxylic acids, they could stabilize the precursor and thus favor the growth, leading to fewer but larger NPs. This idea of controlling the precursor reactivity to tune the NP size was highly inspiring and motivated intensive researches. For instance, G. Xiao et al. reported that the chemical activities of Cu and Se precursors allowed a fine control of the final structure and shape of CuSe NPs.[8] Controlled addition of complexing ligands onto precursors allows forming *in situ* active species or stable complexes to feed the nucleation and growth respectively.[9] In our group Fe,[10] Co[11] and FeCo NPs[2] with controlled size and shape were prepared from amido-based organometallic compounds using carboxylic acids as ligands, stable carboxylate compounds being formed in-situ.

Among the different magnetic materials, Ni combines excellent catalytic properties, competing with noble-metal based catalysts.[12,13,14,15] Due to its higher natural abundance, the synthesis of metallic Ni nanoparticles with controlled size and shape received considerable interest. Among the different strategies, metal-organic chemical routes lead to readily dispersed NPs directly suitable for catalytic reactions. Numerous reaction conditions, such as nature of the Ni precursors,[16] solvents, type and concentration of ligands,[17] have been studied. For instance, isotropic spheres of various sizes were produced from $Ni(acac)_2$ in presence of oleylamine/trioctylphosphine (TOP)[18] or oleic acid/oleylamine,[19] the role of this ligand pairs

being recently extensively reviewed by Mourdikoudis et al.[20] Using a reducing hydrogen atmosphere Ni cubes were grown in the presence of HDA and TOP as surfactants.[21] Regarding shape control, which is highly desired for surface-specific reactions, anisotropic nanoparticles were isolated in some rare cases. For instance, the reduction of $Ni(COD)_2$ in the presence of HDA and trioctylphophineoxide, leads to elongated NPs.[22] Highly anisotropic Ni nanowires were produced by the reduction of a nickel stearate complex under hydrogen, in the presence of HDA/stearic acid.[23] Finally, branched Ni nanoparticles were prepared from nickel acetate under very high hydrogen pressures.[24]

Controlled growth of anisotropic Ni nanoparticles using a simple reaction could allow enhancing the magnetic anisotropy and therefore, the heating efficiency of the particles. Though the specific absorption rate is not directly linked with the performance in catalysis, it allows reaching locally higher temperature and thus activate more demanding catalytic reactions. While FeNi NPs were successfully applied for catalytic reactions in both the gas phase and the liquid phase,[12,25] monometallic Ni NPs could address other reactions providing that the magnetic activation is efficient enough. But, with a fairly low magnetization (55 $A.m^2.kg^{-1}$) and a reduced magnetocrystalline anisotropy (-5×10^3 $J.m^{-3}$), the heating capacity of isotropic Ni NPs is expected to be too low to reach the onset temperature of catalytic reactions such as Fisher-Tropsh. Therefore we report here the synthesis of Ni NPs with tunable size and morphology achieved by the decomposition of a homoleptic Ni(II) amidinate precursor, $[Ni\{MeC(N\textit{i}Pr)_2\}_2]$, in the presence of acid and amine ligands. This Ni amidinate precursor has proven to be a suitable precursor for atomic layer deposition (ALD),[26] due to its high volatility, high thermal stability and properly self-limited reactivity with molecular hydrogen.[27] However, there are only

few examples for its use in liquid-phase synthesis. Apart from our team, which uses it for the synthesis of FeNi NPs,[12,25] metastable Ni NPs exhibiting the hexagonal close-packed structure were reported by the Janiak's group in the presence of ionic liquids.[28] We report here a fairly simple yet highly versatile synthesis leading to a large size and shape control of face-centered cubic Ni NPs, solely playing with the ligand concentration and the reaction atmosphere. The impact of the Ni NP shape onto the magnetic properties was evidenced using conventional magnetometry, calorimetric magnetic hyperthermia and electron holography combined with micromagnetic simulations.

EXPERIMENTAL METHODS.

Chemicals and Materials. All syntheses were performed under argon atmosphere using Fischer-Porter bottles, argon/vacuum lines and glove boxes, due to the air sensitivity of the precursor. Mesitylene (99% Across Organics) and toluene (99%, Fisher), were degassed and transferred in the glove box prior to use. Hexadecylamine (98%) and palmitic acid (99%) were purchased from Sigma Aldrich and used as received. The Ni amidinate precursor, $Ni\{MeC(N\textit{i}Pr)_2\}_2$ ($\textit{i}Pr=C_3H_7$, $Me = CH_3$), was purchased from Nanomeps.

Synthesis of Nickel(0) Nanoparticles. In a typical synthesis of polyhedral NPs, the reaction was prepared in a glove-box filled with Ar. $Ni\{MeC(N\textit{i}Pr)_2\}_2$ (0.4 mmole; 136.5 mg) was dissolved in mesitylene (4 mL) leading to a dark brown solution. A solution of PA (0.8 mmole; 205 mg) in mesitylene (8 mL) was added onto the Ni precursor, leading to a green solution. Then, a solution of HDA (0.4 mmole, 96 mg) in mesitylene (8 mL) was finally added. A color change from green to purple was observed under mild stirring. The concentration of the Ni species remained constant throughout the experiments (20 mM), while the concentration of the ligands was modified to control the final NP size.

The reaction mixture was then transferred into a Fisher-Porter bottle hermetically sealed. The bottle was taken out from the glove box and directly immerged in a preheated oil bath at 150°C. The reaction mixture was magnetically stirred during the 24h of reaction at 150°C. The final nanoparticles were separated by magnetic attraction and washed several times with toluene to remove the excess of ligands (5 mL). The particles were dried under vacuum and stored in powder state in the glove box.

Anisotropic NPs were prepared following the same protocol, the reaction mixture was pressurized under 3 bars of dihydrogen at room temperature prior to being heated at 150°C.

The monitoring of the anisotropic NP reaction was performed by up-scaling the reaction mixture up to 100 mL and splitting it into 5 different Fisher-Porter bottles. After being pressurized under 3 bars of H2, the bottles were let to react in the preheated oil bath for 5 min, 20 min, 1 h, 6 h and 24 h. At the end of the reaction, the bottles were cooled down at room temperature by natural convection. The experiments have been repeated at least three times to confirm their reproducibility. The yield after 24h of reaction was determined considering the total weight of the powder we could isolate (20 ± 1 mg) and the metallic content determined by TGA (95 ± 2 %). Compared to the 24 mg of Ni initially introduced we can deduce a yield of ~ 80%.

Characterization of the NPs. Microscopy samples were prepared by depositing a drop of a diluted colloidal solution on a carbon coated copper grid. The samples were observed on a JEOL-1011 for Bright Field Transmission Electronic Microscopy (TEM) working with 100 kV. In all cases, size histograms were determined by manual counting process over 100 particles, using ImageJ software.[29] Size distributions were fitted by Gaussian law allowing to extract the calculated mean size and the standard deviation σ. High Resolution TEM (HRTEM) was performed on a Cs corrected Hitachi HF3300 microscope (I2TEM) operated at 300 kV. Scanning electron microscopy (SEM) was performed using a JEOL JSM 7800F, operated at 5 kV. The working distance was set at 10 mm.

X-ray diffraction (XRD) patterns were recorded on a PANalytical Empyrean diffractometer using the Co K_α radiation. The XRD samples were prepared in the glove box to prevent any oxidation, the powder being sealed between two Kapton foils.

Thermogravimetric Analysis (TGA) was performed on a Mettler-Toledo balance. The procedure employed to determine the metallic content of the final powder consists in burning and oxidizing the sample under air up to 500°C and then reducing it under a mixture of 4% H_2 – 96% Ar up to 700°C in air and under H_2/Ar atmosphere.

The magnetic properties of the nanoparticles were characterized using a Physical Property Measurement System (PPMS, Quantum Design) in the Vibrating Sample Magnetometer configuration (VSM). ±3T hysteresis measurements were recorded at 300K and 5K after field cooling at 3T to probe the presence of an oxide shell. Nanoparticles were studied in powder state. After normalizing with the metallic content of the powder determined by TGA, the magnetization measured at + 3T (M_{3T}) was compared with the bulk magnetization (55 $A.m^2.kg^{-1}$). Nanoparticles were also studied or as thin film on a 4 mm x 4 mm Si substrate. In that aim, a 6 µL drop of a concentrated suspension was deposited on the substrate and let to evaporate within an electromagnet under a planar external magnetic field $\mu_0 H_{ext}$ = 1T. The deposition is repeated 5 time to obtain a continuous film from which we assumed an in-plane magnetization. The measurements were performed both in-plane and out-of-plane.

Specific absorption rate (SAR) of the Ni nanoparticles was determined by calorimetry. For a typical hyperthermia experiment, 12 mg of Ni nanoparticles were dispersed in 0.5 mL of mesitylene and were introduced under the Ar atmosphere of the glove box in an air-tight tube. The tube was then placed in a calorimeter containing 1.8 mL deionized water at room temperature. The temperature increase of the DI water was monitored during the experiment. The calorimeter was exposed to an alternative magnetic field at a frequency of 93 kHz and a magnitude varying between $\mu_0 H_{rms}$ = 0 to 47 mT for 60 s. The increase in temperature at the end of the magnetic field application was determined after shaking the calorimeter to ensure the temperature homogeneity, which was measured by two probes (at the top and at the bottom of

the calorimeter). The increase in temperature was determined from the mean slope of the $\Delta T/\Delta t$ function. The raw SAR values were calculated using the following expression:

$$SAR = \frac{\sum_i C_{pi} m_i}{m_{Ni}} \times \frac{\Delta T}{\Delta t} \quad \text{(Eq. 2)}$$

were Cp_i and m_i are the specific heat capacity and the mass for each component respectively (Cp = 444 $J.kg^{-1}.K^{-1}$ for Ni, Cp = 1750 $J.kg^{-1}.K^{-1}$ for mesitylene, Cp = 4186 $J.kg^{-1}.K^{-1}$ for water and Cp = 720 $J.kg^{-1}.K^{-1}$ for glass), and m_{Ni} is the mass of pure Ni in the nanoparticles determined by thermogravimetric analysis.

The raw SAR values were corrected from the calorimeter losses, which were previously calibrated using preheated DI water. For the samples presented in this article; the measurement time was of 60 s, corresponding to a correction factor of 1.077.

Off-axis electron holography (EH) is an interferometric technique in transmission electron microscopy (TEM) where the phase shift of an initially coherent electron beam is recorded when interacting with the electromagnetic fields within and around the sample.[30,31,32] Using a Möllenstedt biprism (thin conductive wire where a potential is applied), the part of the beam which has interacted with the object is overlapped with the remaining part which passes through the vacuum. The resulting interference pattern (*i.e.* the hologram) can thus be analyzed to extract the phase shift due to the electromagnetic fields emanating from the specimen.

The expression of the electron beam phase shift ϕ is based on the Aharanov-Bohm equations:

$$\phi(\mathbf{r}) = C_E \int V(\mathbf{r}, z) dz - \frac{e}{\square} B_\perp(\mathbf{r}, z) dr dz \quad \text{(Eq.3)}$$

where **r** is the two-dimensional position vector in the image plane, *z* the direction parallel to the electron beam, C_E a constant related to the energy of the beam ($6.52\ 10^6\ V^{-1}.m^{-1}$ at 300 kV), *V* the electrostatic potential, *e* the electron charge, □ the reduced Planck constant and $B_\perp$ the magnetic induction component perpendicular to the position vector. Electrostatic and magnetic contributions to the phase shift can be separated by recording holograms before and after flipping the specimen: the electrostatic contribution remains the same while the sign of magnetic phase shift reversed. It is important to note that the measured magnetic phase shift corresponds to a

projection and an integration of all in-plane magnetic field contributions along the electron path.[33]

EH was performed using the dedicated Hitachi HF-3300 (I2TEM) microscope operated at 300kV in a corrected Lorentz mode to avoid any magnetic interaction between the Ni particles and the field generated by the objective lens,[34] and using a double biprism setup.[35] The holograms were acquired by applying the π-shift method[36] and using a home-made corrective software to correct for both a drift in interference fringes and of the sample.[37] The exposure time was set to 120 seconds per hologram and an inter-fringe distance of 0.9 nm (6.4 pixels). The resulting resolution of the treated magnetic phase images were extracted by home-made software based on Fourier analysis is 2.7 nm.

Micromagnetic Simulations. Micromagnetic simulations were performed through the 3D version of the micromagnetic code OOMMF version 1.2.0.5, based on the bulk room temperature magnetic parameters of face-centered-cubic nickel: saturation magnetization $M_S = 4.88\times10^5$ A/m, exchange stiffness $A = 10.5\times10^{-12}$ J/m and cubic anisotropy constant $K_1 = -5\times10^3$ J/m^3. Based on the structural characterization by electron microscopy, the branches were introduced as cylinders of 150 nm in length and 24 nm in diameter whereas ellipsoids were added at tips. The Ni pods/nanostars are discretized in 3D cubic cells with 2.5 nm side length. A damping parameter of $\alpha = 0.5$ was used to reach the equilibrium remnant state rapidly. OOMMF provides vector maps of the magnetization M and the dipolar field H_d of the magnetic element. Since electron holography experimentally provides a 2D phase shift map of the nanoparticles corresponding to the magnetic induction defined as $B = \mu_0(H_d + M)$, the magnetization and dipolar field vector coordinates in each cell were summed to obtain the 3D induction map. The phase shift in EH originates from the integration of the magnetic induction along the incident electron beam direction, therefore the calculated induction vectors were then summed along the z direction, *i.e.* the electron beam direction. Finally, for comparison with the experimental phase shift map, a phase shift image was calculated from this 2D induction map using the Aharonov-Bohm relation (Eq. 3). The quantitative agreement between the measured and the simulated phase shift images was not perfect. The thickness being difficult to estimate from TEM image, a second simulation has been performed reducing the branches' thickness by 15%. The four branches were considered as elliptical cylinders of 20 nm thick in the [001] direction.

RESULTS AND DISCUSSION.

Ni nanoparticle synthesis

Ni nanoparticles were prepared by the reduction of an homoleptic Ni(II) amidinate precursor ($Ni\{MeC(N\textit{i}Pr)_2\}_2$]) in the presence of a mixture of amine and acid ligands under mild conditions (150°C, inert atmosphere of Argon). Figure 1 shows the size evolution of the final nanoparticles synthesized as a function of the PA concentration used, the HDA concentration being kept constant at 20 mM, corresponding to an amine:Ni ratio of 1:1.

Small NPs of ~3 nm were synthesized in the presence of 20 mM of PA (Figure 1a and S1). When the acid concentration was set to 40 mM (i.e. corresponding to an acid:Ni ratio = 2:1), large polyhedral NPs were obtained, with a mean length of 16 ± 2 nm (Figure 1b). Increasing further the acid concentration to 60 mM yielded fairly similar polyhedral NPs (Figure 1c). However, the supernatant was still green-colored after 24h, revealing that the reaction was not completed yet. For higher concentrations ([PA]=80 mM), no NP were detected after 24h of reaction, the solution remaining light green as at the very beginning of the reaction.

In the presence of an excess of amine (40mM, corresponding to an amine:Ni ratio = 2:1), similar results were obtained (Figure S1). Small particles were favored at low acid

concentrations ($\leq$ 30 mM), large polyhedral ones were synthesized for [PA] = 40 mM while stable complexes were stabilized at large concentrations ([PA]$\geq$ 60 mM).

Repeating the syntheses with [HDA] = 20 mM and varying the acid concentration under 3 bars of H_2 yield fairly different NPs. For [PA] = 20 mM, fairly polydisperse Ni NPs of 10 ± 2 nm were obtained (Figure 1d). Increasing the acid concentration to 40 mM yield nanorods with an aspect ratio of ~2.5 (Figure 1e, Table 1). In the presence of a large excess of acid, *i.e.* [PA] ≥ 60 mM, fairly big NPs with irregular anisotropic shapes and higher aspect ratios were produced (Figures 1f and S2). Mourdikoudis *et al*. reported fairly similar guitar-like shape NPs by reducing Ni(stearate)$_2$ in pure octadecylamine under H_2.[16] Interestingly, the supernatant were all colorless after 24h of reaction under H_2, even in very large excess of acid ([PA] = 100 mM, Figure S2). One can thus deduce that the stable Ni carboxylate complexes formed *in situ*, which were responsible for the green color observed under Ar, were fully reduced in presence of H_2.

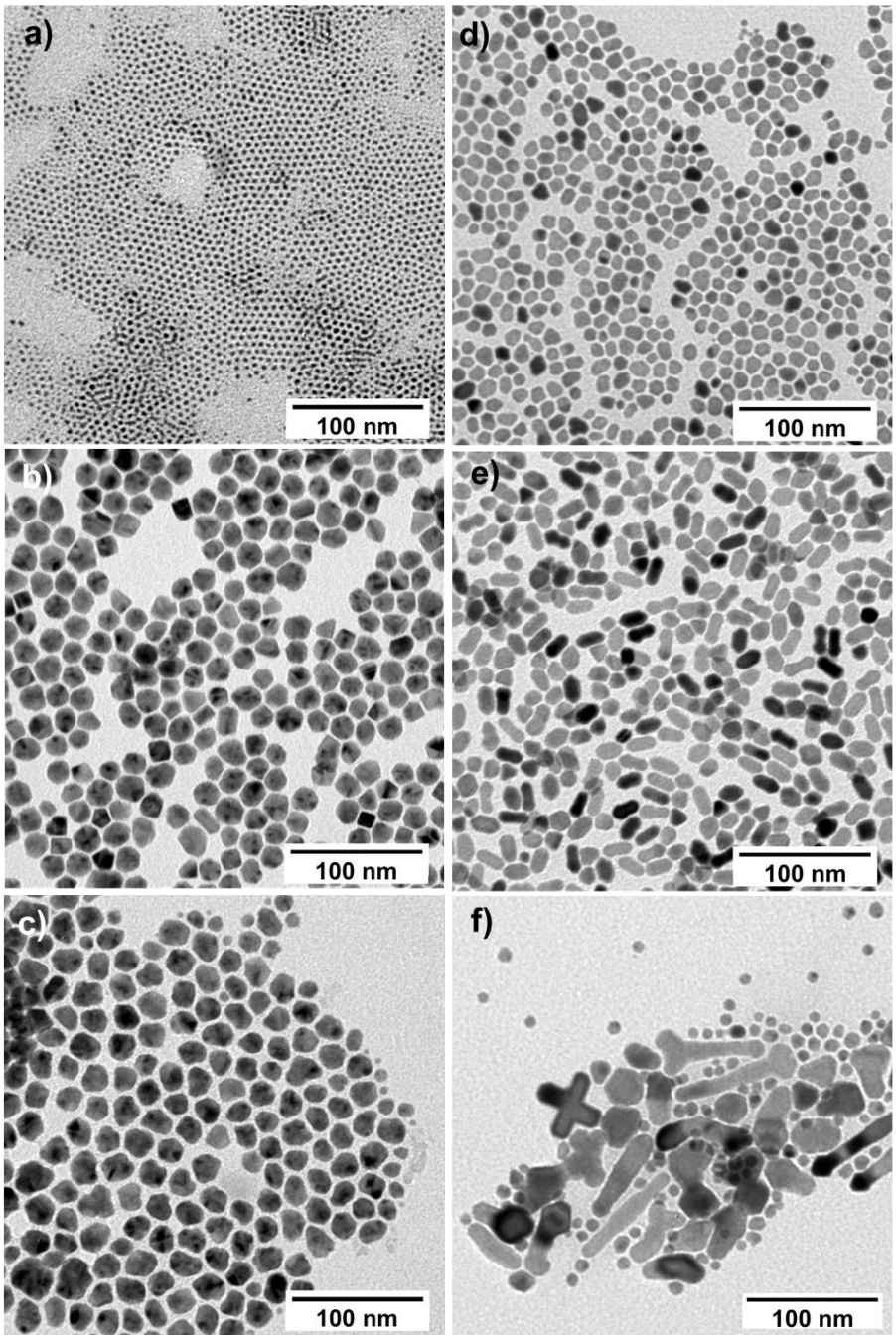

Figure 1. *TEM images of Ni nanoparticles isolated after 24h of reaction at 150°C a-c) under Ar or d-f) under 3 bars of* H_2*. The reaction was performed in presence of [HDA] = 20 mM and [PA] = a,d) 20 mM, b,e) 40 mM, and c,f) 60 mM*

Amines are known to be fairly efficient reducing agents for organometallic complexes.[38] Oleylamine, an unsaturated amine, is the most widely used.[39] Carenco *et al.* prepared for instance Ni nanoparticles by thermal decomposition of $Ni(acac)_2$ in presence of oleylamine.[18] We previously reported that HDA, a saturated amine containing 16 carbons, allowed reducing $\{Fe[N(SiMe_3)_2]_2\}_2$ complex into Fe(0) NPs, thanks to its oxidative transformation into imine.[40] Here, we observed that HDA could reduce Ni(II) amidinate precursor into Ni(0) NPs, the size of which being controlled by the acid concentration. As proposed by Pr. Horst Weller on $CoPt_3$ NPs,[7] we could therefore tune the NP size by controlling the ratio between the reactive Ni species, involved in the nucleation, and the more stable ones formed *in situ* by reaction with PA, which feed the growth. However, in the presence of a large excess of PA (acid:Ni ≥ 3:1), the complexes formed could no longer be reduced by HDA. A stronger reducing agent, namely H_2, was therefore used yielding anisotropic NPs.[41]

Since we combine in the reaction the advantages of both reductants, H_2 and HDA, the exact role of H_2 could be questioned. First, the reaction kinetics in the different conditions were much faster. For instance, in presence of [PA] = 40 mM and [HDA] = 20 mM (Figure 1b and e), the NPs formed after > 6 h under Ar but only few minutes under H_2 as revealed by the black color change. Then, the amine concentration did not affect the mean diameter of the polyhedral NPs obtained with [PA] = 20 mM (Figure S3). If HDA was also acting as a reducing agent, one could expect a modification of size. Finally, in presence of a large excess of PA, the reduction was not observed under Ar, while it is quite fast under H_2. Therefore, we believe that the dominant reductant in the system is H_2, overpassing the HDA reducing force.

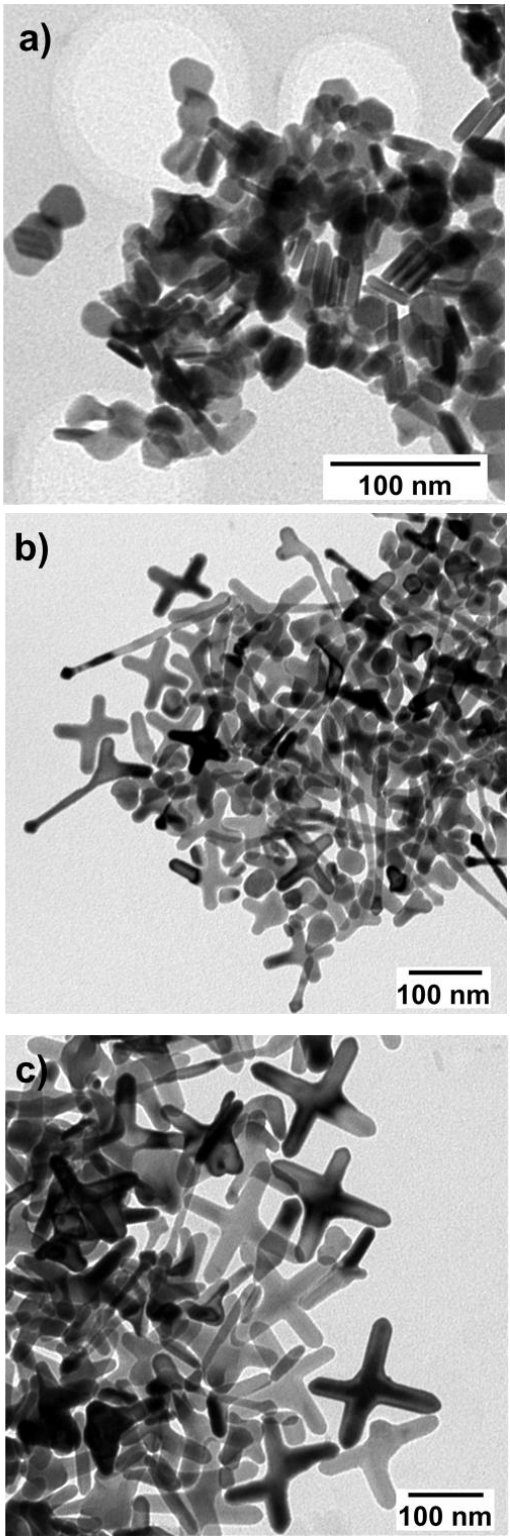

Figure 2. *TEM images of Ni nanoparticles prepared under H2 in presence of [PA] = 100 mM and [HDA] = a) 0, b) 100 mM and c) 200 mM.*

To extend the NP shape control under H_2, a large set of acid and amine concentrations were studied. The most interesting results were obtained in the presence of a large excess of acid ([PA] = 100 mM, acid:Ni = 5:1). In the absence of amine, nano-plates of around 42 nm width × 8 nm thick were produced quantitatively, with a yield exceeding 75% (Figure 2a and S4). A colorless supernatant was observed after 24h of reaction, revealing once more the importance of H_2 to reduce stable Ni compounds. With [HDA] = 100 mM, a mixture of nanorods with guitar-shaped edges and pods (mono, bi, tri, tetra) was observed (Figure 2b). Increasing further the amine concentration to 200 mM allows to stabilize preferentially 140 nm tetrapods (Figure 2c). TEM giving access only to the projected image, scanning electron microscopy was used to probe the 3D configuration of the tetrapods. images evidenced in a very large majority (>80%) a planar structure (Figure S5).

Structural characterization

The different Ni NPs have been characterized by X-Ray diffraction revealing a face-centered-cubic (fcc) Ni structure as expected (Figure S6). The calculated lattice parameter of Ni (a = 3.5231 Å) being in good agreement with the bulk value (a = 3.5238 Å). No sign of impurities or oxides were detected. In the case of the NPs prepared under Ar, crystallite mean sizes much smaller than the mean TEM ones have been determined using Rietveld refinement (Figure S7 and Table S1). These sizes were thus revealing the polycrystalline nature of the polyhedral NPs prepared under Ar. Extending the reaction time up to 3 days leads to larger NPs (up to 25 nm) but with a similar crystallite size (Figure S8 and Table S1), thus recrystallization process could not be promoted at 150°C.

The high quality crystalline structure of the particles prepared under H_2 was statistically measured by XRD. Maud refinement on the XRD pattern of the polyhedral NPs revealed a crystalline size of 10 nm, in good agreement with the TEM mean size (Figures 1d, S9 and Table 1). High-resolution TEM images revealed that the nanorods, prepared with [PA] = 40 mM and [HDA] = 20 mM, were single-crystalline and grew along the <100> direction (Figure 3a and S10). The planar tetrapods prepared in large excess of ligands ([PA] = 100 mM; [HDA] = 200 mM) were also single-crystalline (Figure 3b-c and S10). Surprisingly, the branches did not grow along the <100> directions, as in the case of the rods, but along the <110> directions.

Pr. Chen's group has previously reported very detailed studies on the formation of branched Ni structure in presence of H_2.[24,42] Considering both growth kinetics and surface energies, they provide an open-access program to simulate the stable branched structures.[24] However, such planar tetrapods can not be reached using this program: favouring <110> growth direction would eventually lead to 12-pods structures. While 3D tetrapods[43,42] or octapods grown along <111> direction [24,42] were previously reported, Ni planar tetrapods are indeed fairly rare. LaGrow *et al.* obtained them in a 2% yield along with mono, bi and tripods when decomposing Ni(II) acetylacetonate under H_2 in presence of a mixture HDA/TOP.[44] To the best of our knowledge, this is the first time that planar tetrapods can be quantitatively prepared, with a yield exceeding 80%, using a fairly simple method.

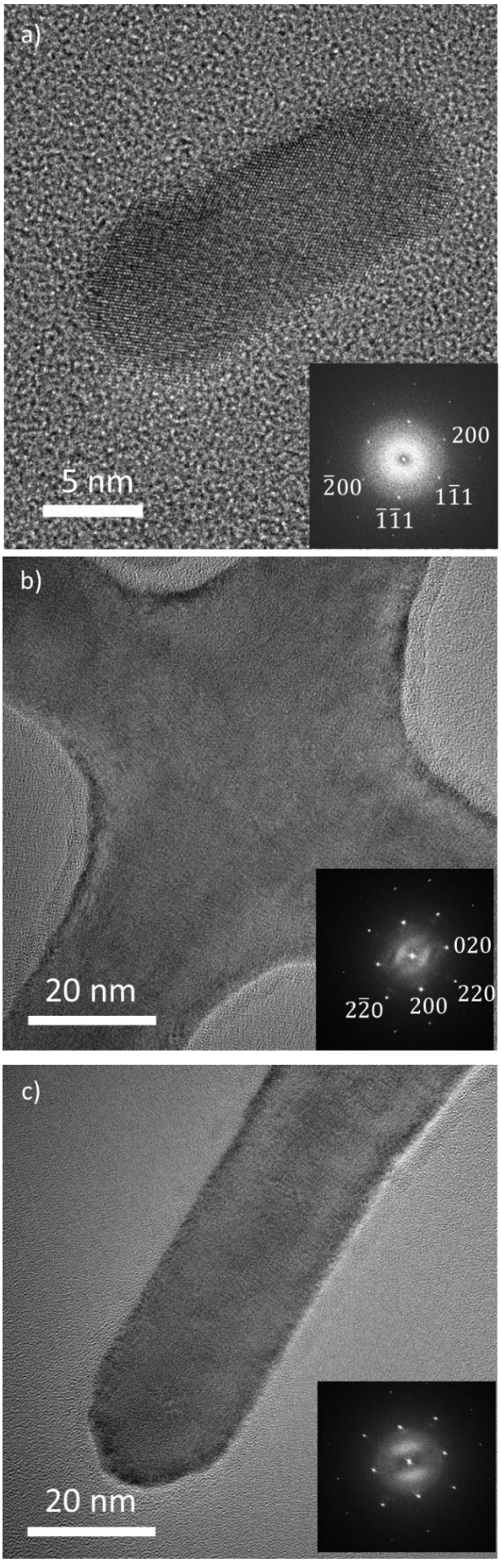
a)
5 nm
200
$\bar{2}00$
$1\bar{1}1$
$\bar{1}\bar{1}1$
b)
20 nm
020
$2\bar{2}0$
200
220
c)
20 nm

Figure 3. *HRTEM images and the corresponding Fourier transforms of a) a nanorod viewed along the <110> zone axis, and the b) central and c) branch part of a planar tetrapod viewed along the <100> zone axis.*

Growth mechanism of planar tetrapods

A kinetic study was therefore performed to further understand the growth of the planar pods. Despite the very large excess of acid (acid:Ni = 5:1) the reaction was quite fast. After 5 min of reaction, tetrapods of 28 nm along with ill-defined NPs were already observed (Figure 4a). After 20 min, the tetrapods reach 80 nm (Figure 4b). The final size was reached after 1h with highly faceted branches (Figure 4c and S12). At that point the supernatant was still light-green coloured, revealing unreacted Ni complexes. After 6h, the supernatant became colorless, the tetrapods' branches appeared thicker and with rounded edges (Figure 4d). Therefore, tetrapods were quickly formed after a fairly fast nucleation process. No sign of oriented attachment of coalescence could be observed while a conventional growth likely fed by the reduction of stable Ni complexes seemed to occur. To understand why only 4 of the <110> growth directions were favoured, one could think of an additional driving force. In the case of Au nanowires prepared in organic medium, a confined growth environment within a lamellar phase was evidenced.[45,46] We have previously reported that PA and HDA could organize to form organic superstructures into which Fe NPs grew.[10] In the presence of a large excess of both ligands, it is reasonable to think that a structuration of the growth medium occurred probably into a lamellar phase.

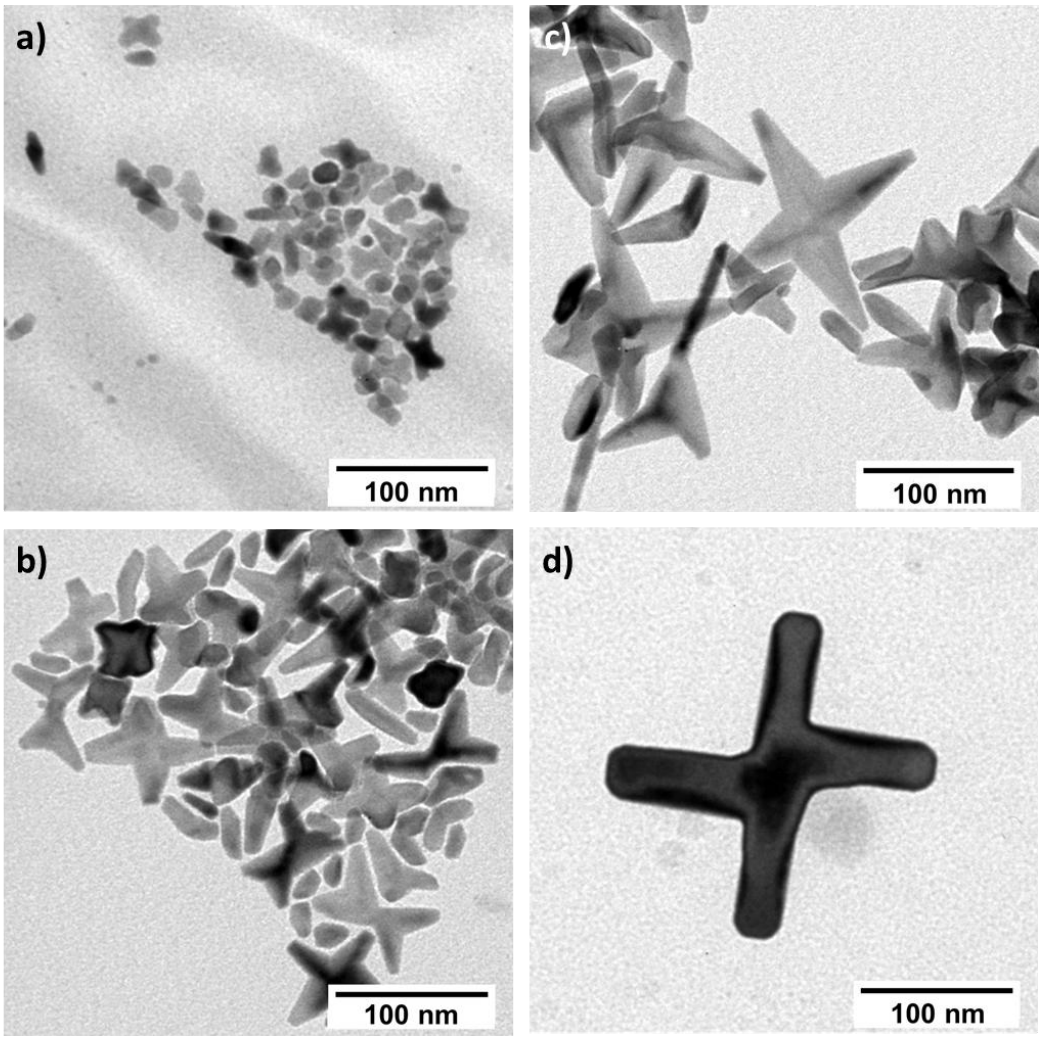

Figure 4. *TEM images of Ni nanoparticles prepared at 150°C under H_2 in presence of [PA] = 100 mM (acid:Ni = 5:1) and [HDA] = 200 mM (amine :Ni = 10 :1) after a) 5 min, b) 20 min, c) 1h and d) 6h of reaction.*

Magnetic characterization of Ni nanoparticles

The magnetic properties of the different Ni NPs were investigated both as powders and as thin films with in-plane magnetization prepared by drop casting under external magnetic field ($\mu_0 H_{ext}$ = 1T). The Ni NPs synthesized in this work display magnetization values of 56 ± 3 $A.m^2.kg^{-1}_{Ni}$ (Figure 5a and Table 1). These values are in agreement to the bulk one (55 $A.m^2.kg^{-1}$)[1] which confirms that the presence of HDA and PA as ligands did not affect the magnetic properties.[10,22]

The NPs were generally ferromagnetic at 300K: despite the soft character of Ni which usually leads to superparamagnetic NPs even at large sizes,[18,47] polyhedral NPs of 15 and 20 nm prepared under Ar had a blocking temperature above 300K as evidence by zero-field cooling field cooling measurements (Figure S13). In addition to the conventional measurement on powders, thin films of Ni NPs were prepared by drop casting under an external magnetic field of 1T (Figure S14). Magnetic measurements were performed in-plane (Figure 5b) and out-of-plane (Figure S15) on the thin films. The films exhibit fairly similar magnetic properties in-plane whatever the orientation of measurement compared to the direction of the applied field (Figure S15a), revealing that the torque induced by the external magnetic field was not strong enough to generate a real alignment of the NPs. However, a difference is observed in the out-of-plane direction, which behaves as a hard axis as one could expect. In every case, the films exhibited a weak coercive field at room temperature which slightly increased with the NP anisotropy (Figure 5b and Table 1): the planar tetrapods, which combine a large size with 2D branches displayed the highest coercive field $\mu_0 H_C$ = 19 mT.

a)

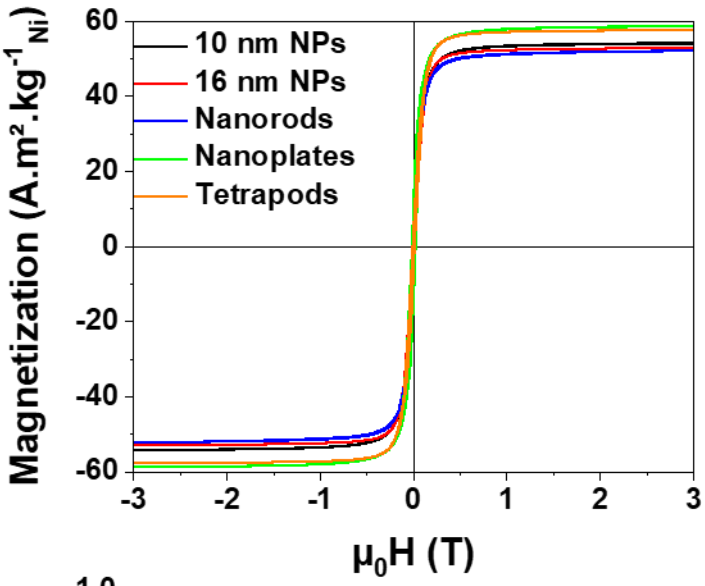
10 nm NPs
16 nm NPs
Nanorods
Nanoplates
Tetrapods
Magnetization (A.m².kg⁻¹Ni)
μ0H (T)

b)

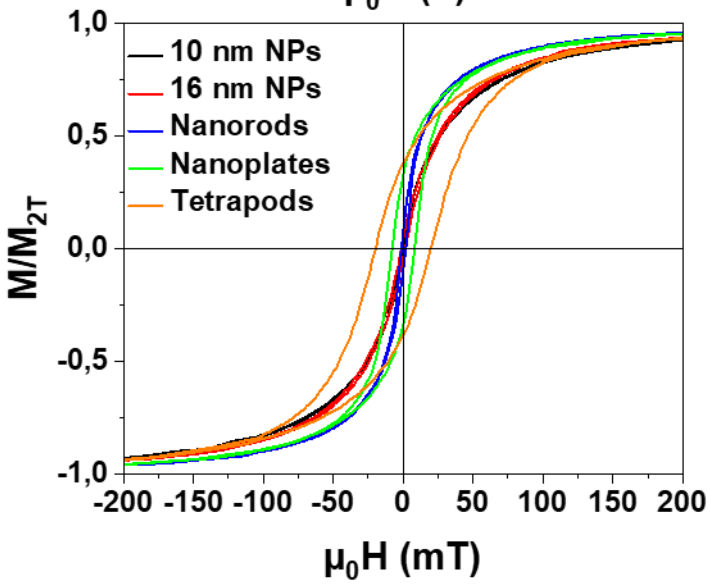
10 nm NPs
16 nm NPs
Nanorods
Nanoplates
Tetrapods
M/M2T
μ0H (mT)

c)

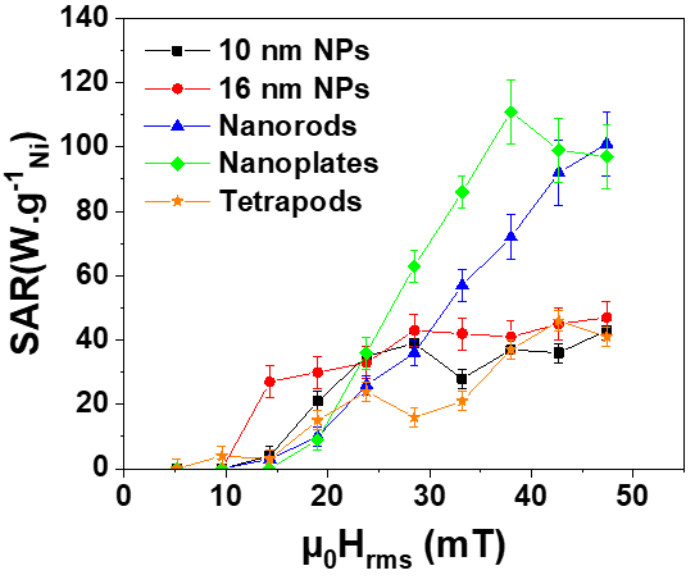
10 nm NPs
16 nm NPs
Nanorods
Nanoplates
Tetrapods
SAR(W.g⁻¹Ni)
μ0Hrms (mT)

Figure 5. *Magnetic hysteresis loops recorded at 300K a) in powder state and b) on film thin along the in-plane hard axis (at 90° of the external field direction used during the drop casting) and c) heating power measurements at 100 kHz and $\mu_0 H_{rms}$=0–47 mT for 10 nm (black, prepared under H_2) and 16 nm polyhedral NPs (red, prepared under Ar), 23×9 nm nanorods (blue), 42×8 nm nanoplates (green) and 140 nm tetrapods (orange).*

Surprisingly, Ni particles were fairly stable under air, no sign of oxidation was detected after 7 days of air exposure neither structurally by XRD and HRTEM (Figures S16 and 3), or magnetically. No exchange bias was observed after field cooling at 5K (Figure S17) and the magnetization remained almost constant (Figure S18). The first signs of oxidation were observed by XRD after 6 month of air exposure (Figure S16).

	[PA] (mM)	[HDA] (mM)	Gas	TEM (nm)	XRD (nm)	M_{3T} ($A.m^2.kg_{Ni}^{-1}$)	$\mu_0 H_C$ (mT)	SAR ($W.g_{Ni}^{-1}$)
Polyhedrons	40	20	Ar	16 ± 2	7	53 ± 5	1	47 ± 5
Nanospheres	20	20	H_2	10 ± 2	10	54 ± 5	1	43 ± 5
Nanorods	40	20	H_2	23 ± 4 (L) × 9 ± 3 (W)	12	52 ± 5	2	100 ± 10
Nanoplates	100	0	H_2	42 ± 9 (W)× 8 ± 4 (T)	20	58 ± 5	8	105 ± 10
Tetrapods	100	200	H_2	140 ± 20 (L) 27 ± 3 (W)	35	57 ± 5	19	46 ± 5

Table 1*. Summary of the structural and magnetic characterization of the different Ni nanoparticles prepared under various experimental conditions. TEM: mean size determined by microscopy. (L): length; (W): width; (T): thickness. XRD: crystallite size determined from Maud refinement of XRD pattern, M_{3T}: magnetization measured in powder state at 300K for $\mu_0 H$ = 3T. $\mu_0 H_C$: coercive field measured at 300K along the hard axis of an oriented thin film. SAR: specific absorption rate measured at f = 93 kHz.*

Heating properties of Ni nanoparticles

Heating power measurements were performed by applying an alternating magnetic field (f = 93 kHz) onto a suspension of Ni nanoparticles (Figure 5c). As previously reported, the NPs tend to align to form needles once the field is on.[48] Despite a comparable volume and fairly similar static magnetic properties, nanorods delivered an heating efficiency two times higher than the polyhedrons (100 $W.g^{-1}$ vs 43 $W.g^{-1}$, Table 1). As initially assumed, the anisotropy allows indeed to finely tune the heating capability of NPs. Of course, these values were still much lower than the heating efficiency of Fe-based NPs previously designed in our group (up to 3000 $W.g^{-1}$).[4,49] However these Ni NPs could be employed in specific catalytic processes that require low reaction temperature in order to control the selectivity of the products.

Surprisingly, the specific absorption rate of planar tetrapods was fairly moderate (48 $W.g^{-1}$) even though they exhibit the largest coercive field ($\mu_0 H_C$ = 19 mT). The magnetic configuration within such 2D object was thus further studied to understand this discrepancy.

Magnetic configuration within individual planar tetrapod

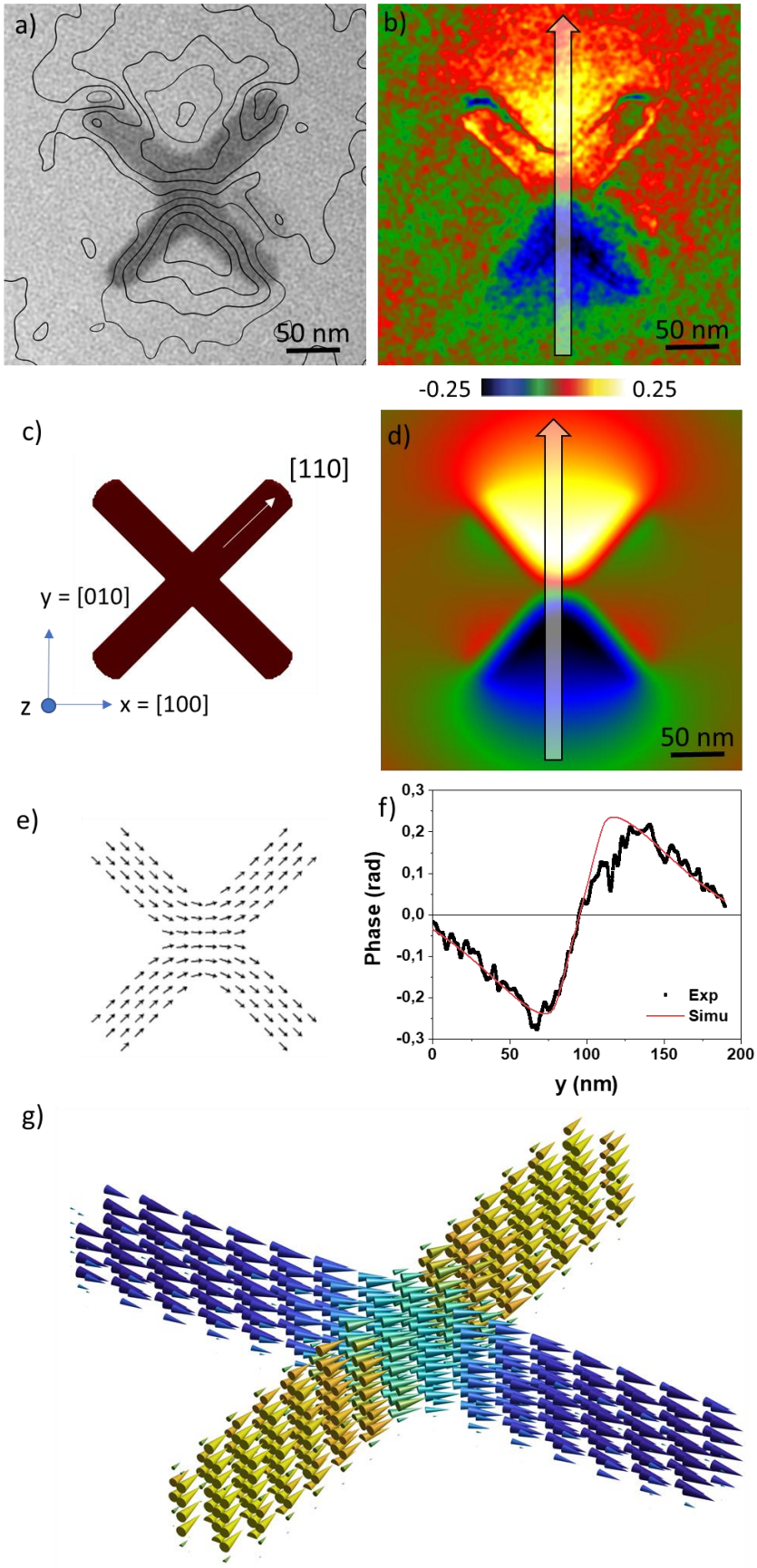
a)
50 nm
b)
50 nm
-0.25
0.25
c)
[110]
y = [010]
z
x = [100]
d)
50 nm
e)
f)
Phase (rad)
0,3
0,2
0,1
0,0
-0,1
-0,2
-0,3
0
50
100
150
200
y (nm)
Exp
Simu
g)

Figure 6. *a) Magnetic induction flux lines superimposed with conventional TEM image contrast and determined from b) the experimental magnetic phase map. The phase step between each contour is equal to 50 mrad for a small overall magnetic phase shift of 0.5 rad. c) Planar tetrapod geometry considered for simulation, branches were along the <110> crystallographic directions as determined by HRTEM. d) Magnetic phase map calculated from e) the stable magnetic configuration determined by micromagnetic simulation considering bulk Ni parameters. f) Measured and simulated phase shift profiles taken along the arrows in (b) and (d). g) 3D view of the magnetic configuration simulated.*

Electron holography (EH) experiments have been carried out on different isolated Ni tetrapods. Results presented on figure 6 are representative of those obtained on all the tetrapods studied by EH. The amplitude image and the magnetic phase map are presented in Figure 6a and b, respectively. Isophase contours, which are parallel to the magnetic induction flux lines, have been calculated from the experimental phase image and added onto the amplitude image for clarity. The projected magnetic induction presents a butterfly-like shape, combining a symmetric axis along the [010] crystallographic direction and an antisymmetric axis along the [100] direction. The branches of the nanoparticle are magnetically coupled two by two: the magnetic induction which enters in the upper left branch exits through the upper right branch; and so does it for the lower branches. It is interesting to note that the magnetic flux is parallel to the branch axis, *i.e.* according to a <110> crystallographic direction, while the expected easy axis for magnetization is along a <111> direction if one considers only the magnetocrystalline contribution. In the tetrapod center, the magnetic flux curved and aligned along the [100] direction.

Micromagnetic simulations have been performed considering an isolated Ni tetrapod. As determined using HRTEM, it was defined as a single crystal with branches along the <110> directions of the *fcc* Ni crystal. Magnetic configurations have been calculated at remanence after

saturating the tetrapod along four different directions of the magnetic field: <100>, <001>, <110> and <111>. The remanent configurations were strictly the same and revealed magnetic moments aligned along the branch axis (Figures 6e and 6g). The simulated phase map (Figure 6d) is in very good agreement with the experimental one, as evidenced by the phase profile on Figure 6f. Note that another magnetic configuration could sometimes be observed starting from of an initial random state, however it is of higher energy compared to the remanence state. Therefore, we conclude that the configuration obtained at remanence, independently of the applied field direction, corresponds to the ground state of such Ni tetrapods. Its experimental evidence in electron holography for all the tetrapods is consistent with their magnetic history, these objects being previously magnetically attracted from the mother liquor along different directions.

The alignment of the magnetic moment along the branch axis could be quite surprising. For *fcc* Ni, the magnetocrystalline anisotropy energy is minimized along <111> directions which are here located out of the pod plane. This configuration is related to the shape of the particle, the dipolar and exchange contributions acting as major energy terms within such planar tetrapod. As a result, this lowest energy magnetic configuration is illustrated by pairs of branches acting as symmetric magnetic flux circulators around the core homogenously magnetized. Although the magnetic configuration exhibited by the tetrapod cannot strictly be considered as a single domain one, since the direction of induction varies within the particle, it is hardly a multidomain one neither, no identifiable domain separation, as walls or vortex, being observed.[50,51] This magnetic configuration could explain the low heating properties of the tetrapods, pure single-domain NPs being far more efficient.

CONCLUSIONS.

Ni nanoparticles displaying a very good size and shape control were prepared through the reduction of an Ni(II) amidinate precursor in presence of amine and acid ligands. HDA was directly used as soft reducing agent to yield polycrystalline NPs but failed in reducing the fairly stable Ni complex formed *in situ* in the presence of PA. A fairly mild pressure of dihydrogen allowed overpassing this limitation, yielding anisotropic NPs, the size of which increasing with the acid concentration. Planar tetrapods were even synthesized quantitatively in the presence of a large excess of ligands. The branches grew along 4 of the 12 possible <110> directions. Combining electron holography in a dedicated microscope and micromagnetic simulations allowed revealing that shape anisotropy overpasses magnetocrystalline anisotropy within Ni tetrapods, leading to an unusual magnetic configuration aligned with the branches. Tuning the shape anisotropy was a fairly efficient mean of controlling the static and dynamic magnetic properties of Ni nanoparticles. The improved heating capabilities observed in Ni nanorods open promising perspectives for magnetically-induced catalysis.

ASSOCIATED CONTENT

Supporting Information. Additional TEM images of Ni NP prepared under Ar and under H_2; Maud refinement of XRD patterns; additional HRTEM images of Ni nanorods and tetrapods; SEM images of tetrapods prepared after 1h and 24h; Additional magnetic measurements are

available free of charge.

AUTHOR INFORMATION

Corresponding Author

* Lise-Marie Lacroix, lmlacroi@insa-toulouse.fr, Tel: +33567048833, Fax: +33561559697

Author Contributions

The manuscript was written through contributions of all authors.

ACKNOWLEDGMENT

This work was supported by the Fondation de la Maison de la Chimie, the French national project POMADE (ANR 19-CE09-0021-01), the EUR grant NanoX n° ANR-17-EURE-0009 in the framework of the « Programme des Investissements d'Avenir" and prematuration programs of the SATT TTT (Soft Magneto) and the Occitanie region (SoftRF). This work has been supported by the European Union Horizon 2020 research and innovation programme under grant agreement No. 823717 – ESTEEM3, the French National Research Agency under the "Investissement d'Avenir" program reference No. ANR-10-EQPX-38-01, and the French national project IODA (ANR-17-CE24-0047). Angélique Gillet and Adeline Pham are warmly thanked for their help for chemical synthesis and Anne Bernand-Mantel for her careful reading of the article and advices on the magnetism section.

ABBREVIATIONS

PA : palmitic acid. HDA: hexadecylamine. TOP : Trioctylphosphine. COD : 1,5-cyclooctadiene. acac : acetylacetonate. TEM : transmission electron microscopy. SEM : scanning electron microscopy. HRTEM : high resolution TEM. NPs : nanoparticles. EH : electron holography. SAR : Specific Absorption Rate. XRD : X-Ray Diffraction. VSM : Vibrating Sample Magnetometry. H_2 : dihydrogen.

REFERENCES

(1) Coey, J. M. D. *Magnetism and Magnetic Materials*; Cambridge University Press: Cambridge, 2010.

(2) Garnero, C.; Lepesant, M.; Garcia-Marcelot, C.; Shin, Y.; Meny, C.; Farger, P.; Warot-Fonrose, B.; Arenal, R.; Viau, G.; Soulantica, K. et al. Chemical Ordering in Bimetallic FeCo Nanoparticles: From a Direct Chemical Synthesis to Application As Efficient High-Frequency Magnetic Material. *Nano Lett.* **2019**, *19* (2), 1379–1386. https://doi.org/10.1021/acs.nanolett.8b05083.

(3) Lacroix, L.-M.; Ho, D.; Sun, S. Magnetic Nanoparticles as Both Imaging Probes and Therapeutic Agents. *Curr. Top. Med. Chem.* **2010**, *10* (12), 1184–1197.

(4) Bordet, A.; Lacroix, L.-M.; Fazzini, P.-F.; Carrey, J.; Soulantica, K.; Chaudret, B. Magnetically Induced Continuous CO $_2$ Hydrogenation Using Composite Iron Carbide Nanoparticles of Exceptionally High Heating Power. *Angew. Chem. Int. Ed.* **2016**, *55* (51), 15894–15898. https://doi.org/10.1002/anie.201609477.

(5) Rajan, A.; Sahu, N. K. Review on Magnetic Nanoparticle-Mediated Hyperthermia for Cancer Therapy. *J. Nanoparticle Res.* **2020**, *22* (11), 319. https://doi.org/10.1007/s11051-020-05045-9.

(6) Carrey, J.; Mehdaoui, B.; Respaud, M. Simple Models for Dynamic Hysteresis Loop Calculations of Magnetic Single-Domain Nanoparticles: Application to Magnetic Hyperthermia Optimization. *J. Appl. Phys.* **2011**, *109* (8), 083921. https://doi.org/10.1063/1.3551582.

(7) Shevchenko, E. V.; Talapin, D. V.; Schnablegger, H.; Kornowski, A.; Festin, Ö.; Svedlindh, P.; Haase, M.; Weller, H. Study of Nucleation and Growth in the Organometallic Synthesis of Magnetic Alloy Nanocrystals: The Role of Nucleation Rate in Size Control of CoPt $_3$ Nanocrystals. *J. Am. Chem. Soc.* **2003**, *125* (30), 9090–9101. https://doi.org/10.1021/ja029937l.

(8) Xiao, G.; Ning, J.; Liu, Z.; Sui, Y.; Wang, Y.; Dong, Q.; Tian, W.; Liu, B.; Zou, G.; Zou, B. Solution Synthesis of Copper Selenide Nanocrystals and Their Electrical Transport Properties. *CrystEngComm* **2012**, *14* (6), 2139. https://doi.org/10.1039/c2ce06270d.

(9) Heuer-Jungemann, A.; Feliu, N.; Bakaimi, I.; Hamaly, M.; Alkilany, A.; Chakraborty, I.; Masood, A.; Casula, M. F.; Kostopoulou, A.; Oh, E. et al The Role of Ligands in the Chemical Synthesis and Applications of Inorganic Nanoparticles. *Chem. Rev.* **2019**, *119* (8), 4819–4880. https://doi.org/10.1021/acs.chemrev.8b00733.

(10) Lacroix, L.-M.; Lachaize, S.; Falqui, A.; Respaud, M.; Chaudret, B. Iron Nanoparticle Growth in Organic Superstructures. *J. Am. Chem. Soc.* **2009**, *131* (2), 549–557. https://doi.org/10.1021/ja805719c.
(11) Estrader, M.; Soulantica, K.; Chaudret, B. Organometallic Synthesis of Magnetic Metal Nanoparticles. *Angew. Chem. Int. Ed.* **2022**, *61* (35). https://doi.org/10.1002/anie.202207301.
(12) De Masi, D.; Asensio, J. M.; Fazzini, P.; Lacroix, L.; Chaudret, B. Engineering Iron–Nickel Nanoparticles for Magnetically Induced CO $_2$ Methanation in Continuous Flow. *Angew. Chem. Int. Ed.* **2020**, *59* (15), 6187–6191. https://doi.org/10.1002/anie.201913865.
(13) Abboud, M.; Alnefaie, R.; Alhanash, A. Unsupported and Silica-Supported Nickel Nanoparticles: Synthesis and Application in Catalysis. *J. Nanoparticle Res.* **2022**, *24* (2), 21. https://doi.org/10.1007/s11051-021-05350-x.
(14) Vij, V.; Sultan, S.; Harzandi, A. M.; Meena, A.; Tiwari, J. N.; Lee, W. G.; Yoon, T.; Kim, K. S. Nickel–Based Electrocatalysts for Energy Related Applications: Oxygen Reduction, Oxygen Evolution, and Hydrogen Evolution Reactions. *ACS Catal.* **2017**, *7*, 7196–7225. https://doi.org/10.1021/acscatal.7b01800.
(15) Zhou, Y.; Martín, A. J.; Dattila, F.; Xi, S.; López, N.; Pérez-Ramírez, J.; Yeo, B. S. Long-Chain Hydrocarbons by CO2 Electroreduction Using Polarized Nickel Catalysts. *Nat. Catal.* **2022**, *5* (6), 545–554. https://doi.org/10.1038/s41929-022-00803-5.
(16) Mourdikoudis, S.; Collière, V.; Amiens, C.; Fau, P.; Kahn, M. L. Metal–Organic Pathways for Anisotropic Growth of a Highly Symmetrical Crystal Structure: Example of the Fcc Ni. *Langmuir* **2013**, *29* (44), 13491–13501. https://doi.org/10.1021/la402001t.
(17) Donegan, K. P.; Godsell, J. F.; Otway, D. J.; Morris, M. A.; Roy, S.; Holmes, J. D. Size-Tuneable Synthesis of Nickel Nanoparticles. *J. Nanoparticle Res.* **2012**, *14* (1), 670. https://doi.org/10.1007/s11051-011-0670-y.
(18) Carenco, S.; Boissière, C.; Nicole, L.; Sanchez, C.; Le Floch, P.; Mézailles, N. Controlled Design of Size-Tunable Monodisperse Nickel Nanoparticles. *Chem. Mater.* **2010**, *22* (4), 1340–1349. https://doi.org/10.1021/cm902007g.
(19) Winnischofer, H.; Rocha, T. C. R.; Nunes, W. C.; Socolovsky, L. M.; Knobel, M.; Zanchet, D. Chemical Synthesis and Structural Characterization of Highly Disordered Ni Colloidal Nanoparticles. *ACS Nano* **2008**, *2* (6), 1313–1319. https://doi.org/10.1021/nn700152w.
(20) Mourdikoudis, S.; Menelaou, M.; Fiuza-Maneiro, N.; Zheng, G.; Wei, S.; Pérez-Juste, J.; Polavarapu, L.; Sofer, Z. Oleic Acid/Oleylamine Ligand Pair: A Versatile Combination in the Synthesis of Colloidal Nanoparticles. *Nanoscale Horiz.* **2022**, *7* (9), 941–1015. https://doi.org/10.1039/D2NH00111J.
(21) LaGrow, A. P.; Ingham, B.; Cheong, S.; Williams, G. V. M.; Dotzler, C.; Toney, M. F.; Jefferson, D. A.; Corbos, E. C.; Bishop, P. T.; Cookson, J. et al.. Synthesis, Alignment, and Magnetic Properties of Monodisperse Nickel Nanocubes. *J. Am. Chem. Soc.* **2012**, *134* (2), 855–858. https://doi.org/10.1021/ja210209r.
(22) Cordente, N.; Amiens, C.; Chaudret, B.; Respaud, M.; Senocq, F.; Casanove, M.-J. Chemisorption on Nickel Nanoparticles of Various Shapes: Influence on Magnetism. *J. Appl. Phys.* **2003**, *94* (10), 6358. https://doi.org/10.1063/1.1621081.
(23) Drisko, G. L.; Gatel, C.; Fazzini, P.-F.; Ibarra, A.; Mourdikoudis, S.; Bley, V.; Fajerwerg, K.; Fau, P.; Kahn, M. Air-Stable Anisotropic Monocrystalline Nickel Nanowires Characterized Using Electron Holography. *Nano Lett.* **2018**, *18* (3), 1733–1738. https://doi.org/10.1021/acs.nanolett.7b04791.

(24) Wang, X.; Liu, N.; Dai, C.; Xu, R.; Wu, B.; Yu, G.; Chen, B. Kinetic Understanding of Hydrogen-Mediated Ni Growth: From Metal Precursor Reduction to Branched Nanostructure Formation. *J. Phys. Chem. C* **2020**, *124* (3), 2160–2170. https://doi.org/10.1021/acs.jpcc.9b09443.
(25) Mustieles Marin, I.; De Masi, D.; Lacroix, L.-M.; Fazzini, P.-F.; van Leeuwen, P. W. N. M.; Asensio, J. M.; Chaudret, B. Hydrodeoxygenation and Hydrogenolysis of Biomass-Based Materials Using FeNi Catalysts and Magnetic Induction. *Green Chem.* **2021**, *23* (5), 2025–2036. https://doi.org/10.1039/D0GC03495A.
(26) Lim, B. S.; Rahtu, A.; Gordon, R. G. Atomic Layer Deposition of Transition Metals. *Nat. Mater.* **2003**, *2* (11), 749–754. https://doi.org/10.1038/nmat1000.
(27) Lim, B. S.; Rahtu, A.; Park, J.-S.; Gordon, R. G. Synthesis and Characterization of Volatile, Thermally Stable, Reactive Transition Metal Amidinates. *Inorg. Chem.* **2003**, *42* (24), 7951–7958. https://doi.org/10.1021/ic0345424.
(28) Wegner, S.; Rutz, C.; Schütte, K.; Barthel, J.; Bushmelev, A.; Schmidt, A.; Dilchert, K.; Fischer, R. A.; Janiak, C. Soft, Wet-Chemical Synthesis of Metastable Superparamagnetic Hexagonal Close-Packed Nickel Nanoparticles in Different Ionic Liquids. *Chem. - Eur. J.* **2017**, *23* (26), 6330–6340. https://doi.org/10.1002/chem.201605251.
(29) Schneider, C. A.; Rasband, W. S.; Eliceiri, K. W. NIH Image to ImageJ: 25 Years of Image Analysis. *Nat. Methods* **2012**, *9* (7), 671–675. https://doi.org/10.1038/nmeth.2089.
(30) Tonomura, A. Applications of Electron Holography. *Rev. Mod. Phys.* **1987**, *59* (3), 639–669. https://doi.org/10.1103/RevModPhys.59.639.
(31) Gatel, C.; Lubk, A.; Pozzi, G.; Snoeck, E.; Hÿtch, M. Counting Elementary Charges on Nanoparticles by Electron Holography. *Phys. Rev. Lett.* **2013**, *111* (2), 025501. https://doi.org/10.1103/PhysRevLett.111.025501.
(32) Gatel, C.; Warot-Fonrose, B.; Biziere, N.; Rodríguez, L. A.; Reyes, D.; Cours, R.; Castiella, M.; Casanove, M. J. Inhomogeneous Spatial Distribution of the Magnetic Transition in an Iron-Rhodium Thin Film. *Nat. Commun.* **2017**, *8* (1), 15703. https://doi.org/10.1038/ncomms15703.
(33) Dunin-Borkowski, R.; Kovacs, A.; Kasama, T.; McCartney, M. R.; Smith, D. J. Electron Holography. In *Springer Handbook of Microscopy*; 2019; pp 767–818.
(34) Snoeck, E.; Houdellier, F.; Taniguch, Y.; Masseboeuf, A.; Gatel, C.; Nicolai, J.; Hytch, M. Off-Axial Aberration Correction Using a B-COR for Lorentz and HREM Modes. *Microsc. Microanal.* **2014**, *20* (S3), 932–933. https://doi.org/10.1017/S1431927614006382.
(35) Harada, K.; Tonomura, A.; Togawa, Y.; Akashi, T.; Matsuda, T. Double-Biprism Electron Interferometry. *Appl. Phys. Lett.* **2004**, *84* (17), 3229–3231. https://doi.org/10.1063/1.1715155.
(36) Volkov, V. V.; Han, M. G.; Zhu, Y. Double-Resolution Electron Holography with Simple Fourier Transform of Fringe-Shifted Holograms. *Ultramicroscopy* **2013**, *134*, 175–184. https://doi.org/10.1016/j.ultramic.2013.06.018.
(37) Gatel, C.; Dupuy, J.; Houdellier, F.; Hÿtch, M. J. Unlimited Acquisition Time in Electron Holography by Automated Feedback Control of Transmission Electron Microscope. *Appl. Phys. Lett.* **2018**, *113* (13), 133102. https://doi.org/10.1063/1.5050906.
(38) Yon, A. M.; Marty, B. J.-D.; Ciuculescu-Pradines, C. D. CHAPTER 6. Amines and Amine-Boranes. In *Nanoscience & Nanotechnology Series*; Mourdikoudis, S., Ed.; Royal Society of Chemistry: Cambridge, 2021; pp 130–156. https://doi.org/10.1039/9781839163623-00130.

(39) Mourdikoudis, S.; Liz-Marzán, L. M. Oleylamine in Nanoparticle Synthesis. *Chem. Mater.* **2013**, *25* (9), 1465–1476. https://doi.org/10.1021/cm4000476.
(40) Meffre, A.; Lachaize, S.; Gatel, C.; Respaud, M.; Chaudret, B. Use of Long Chain Amine as a Reducing Agent for the Synthesis of High Quality Monodisperse Iron(0) Nanoparticles. *J. Mater. Chem.* **2011**, *21* (35), 13464. https://doi.org/10.1039/c1jm12127h.
(41) Yi, D.; Chaudret, B.; Soulantica, K. CHAPTER 5. Gases. In *Nanoscience & Nanotechnology Series*; Mourdikoudis, S., Ed.; Royal Society of Chemistry: Cambridge, 2021; pp 97–129. https://doi.org/10.1039/9781839163623-00097.
(42) Liang, X.; Liu, N.; Qiu, H.; Zhang, C.; Mei, D.; Chen, B. Hydrogen Assisted Synthesis of Branched Nickel Nanostructures: A Combined Theoretical and Experimental Study. *Phys Chem Chem Phys* **2017**, *19* (39), 26718–26727. https://doi.org/10.1039/C7CP04673A.
(43) Shviro, M.; Zitoun, D. Nickel Nanocrystals: Fast Synthesis of Cubes, Pyramids and Tetrapods. *RSC Adv* **2013**, *3* (5), 1380–1387. https://doi.org/10.1039/C2RA22024E.
(44) LaGrow, A. P.; Cheong, S.; Watt, J.; Ingham, B.; Toney, M. F.; Jefferson, D. A.; Tilley, R. D. Can Polymorphism Be Used to Form Branched Metal Nanostructures? *Adv. Mater.* **2013**, *25* (11), 1552–1556. https://doi.org/10.1002/adma.201204366.
(45) Lu, X.; Yavuz, M. S.; Tuan, H.-Y.; Korgel, B. A.; Xia, Y. Ultrathin Gold Nanowires Can Be Obtained by Reducing Polymeric Strands of Oleylamine−AuCl Complexes Formed via Aurophilic Interaction. *J. Am. Chem. Soc.* **2008**, *130* (28), 8900–8901. https://doi.org/10.1021/ja803343m.
(46) Huo, Z.; Tsung, C.; Huang, W.; Zhang, X.; Yang, P. Sub-Two Nanometer Single Crystal Au Nanowires. *Nano Lett.* **2008**, *8* (7), 2041–2044. https://doi.org/10.1021/nl8013549.
(47) Cordente, N.; Respaud, M.; Senocq, F.; Casanove, M.-J.; Amiens, C.; Chaudret, B. Synthesis and Magnetic Properties of Nickel Nanorods. *Nano Lett.* **2001**, *1* (10), 565–568. https://doi.org/10.1021/nl0100522.
(48) Asensio, J. M.; Marbaix, J.; Mille, N.; Lacroix, L.-M.; Soulantica, K.; Fazzini, P.-F.; Carrey, J.; Chaudret, B. To Heat or Not to Heat: A Study of the Performances of Iron Carbide Nanoparticles in Magnetic Heating. *Nanoscale* **2019**, *11* (12), 5402–5411. https://doi.org/10.1039/C8NR10235J.
(49) Marbaix, J.; Mille, N.; Lacroix, L.-M.; Asensio, J. M.; Fazzini, P.-F.; Soulantica, K.; Carrey, J.; Chaudret, B. Tuning the Composition of FeCo Nanoparticle Heating Agents for Magnetically Induced Catalysis. *ACS Appl. Nano Mater.* **2020**, *3* (4), 3767–3778. https://doi.org/10.1021/acsanm.0c00444.
(50) Bonilla, F. J.; Lacroix, L.-M.; Blon, T. Magnetic Ground States in Nanocuboids of Cubic Magnetocrystalline Anisotropy. *J. Magn. Magn. Mater.* **2017**, *428*, 394–400. https://doi.org/10.1016/j.jmmm.2016.12.069.
(51) Guo, S.; Henschel, M.; Wolf, D.; Pohl, D.; Lubk, A.; Blon, T.; Neu, V.; Leistner, K. Size-Specific Magnetic Configurations in Electrodeposited Epitaxial Iron Nanocuboids: From Landau Pattern to Vortex and Single Domain States. *Nano Lett.* **2022**, *22* (10), 4006–4012. https://doi.org/10.1021/acs.nanolett.2c00607.

TOC Graphic